

Interface enhanced photogalvanic effects in the MoSi_2N_4 monolayer for spintronics

Yiming Wang, Yiqun Xie *, Guoli Lin, and Xiang Ye

Department of Physics, Shanghai Normal University, 100 Guilin Road, Shanghai 200234, People's Republic of China



(Received 22 February 2024; revised 21 May 2024; accepted 17 June 2024; published 1 July 2024)

The electrode-semiconductor interface plays an important role in generating and enhancing the photogalvanic effects (PGEs) in semiconducting materials. However, knowledge of the impact of the interface on the PGE for spintronics is currently very limited. Here, we propose the two-dimensional (2D) photodetectors composed of nonmagnetic semiconductor MoSi_2N_4 sandwiched between the half-metallic electrodes of 2D VSi_2N_4 (NbSi_2N_4) and investigate the PGE induced by linear polarized light in the visible range. The $\text{VSi}_2\text{N}_4/\text{MoSi}_2\text{N}_4$ and $\text{NbSi}_2\text{N}_4/\text{MoSi}_2\text{N}_4$ interfaces cause an opposite bending of the conduction bands in MoSi_2N_4 , respectively, due to the different work functions of the two electrodes. This results in a larger and fully-spin-polarized PGE photocurrent for the photodetector with the VSi_2N_4 electrodes, while a much smaller photocurrent with a lower spin polarization for the photodetector with the NbSi_2N_4 electrodes. Meanwhile, both the photodetectors possess a perfect spin-valve effect with a 100% magnetoresistance ratio in a broad visible range. These results suggest that, by using the magnetic electrodes with an appropriate work function, both the magnitude and the spin-polarization of the photocurrent can be largely enhanced, making it promising for the application of the PGE in spintronic devices.

DOI: [10.1103/PhysRevMaterials.8.074002](https://doi.org/10.1103/PhysRevMaterials.8.074002)

I. INTRODUCTION

The photogalvanic effect (PGE) [1–4], namely, the bulk photovoltaic effect [5–10], occurs in materials without space-inversion symmetry and produces a dc photocurrent under illumination of polarized light without the need for any external electrical fields (at zero bias) or p - n junctions. Recent studies have proposed that the PGE in various systems can generate fully spin-polarized photocurrent [11], pure spin current [12,13], and high photocurrent magnetoresistance ratio [14,15], suggesting promising application in spintronics.

The photocurrent generated in the PGE varies with light polarization (helicity), determined by material symmetry, which can be understood from a phenomenological theory [16]. Moreover, the PGE can be treated as a second-order optical response, and therefore the photocurrent is quantitatively calculated by using first-principles methods [17–20]. Within this framework, the PGEs have been investigated in various materials, including the two-dimensional (2D) ferroelectric VSe_2 [21], As [22], V [23] and TlNbX_4O monolayers [24], 2D antimagnetic CrI_3 [13], and heteronodal-line systems [6]. These methods are suitable for the PGE in bulk systems with periodicity but are not applicable to the PGE in the device, which is an open system without periodicity.

In a photoelectric device, e.g., a photodetector, metallic electrodes are indispensable to conduct the photocurrent generated in semiconductor to the outside circuit. The electrodes-semiconductor interface can generate a Schottky electric field to break local inversion symmetry of the semiconductor in a device and therefore produces a robust PGE

under the illumination of polarized light, as has been demonstrated in silicon nanowires [25], WS_2 nanotubes [26], and MoSe_2 monolayers [27]. The electrode-semiconductor interface leads to the band-bending of the semiconductor, yielding a Schottky barrier. Therefore, by choosing metallic electrodes with an appropriate work function to change the barrier height, the PGE photocurrent can be largely enhanced, as has been demonstrated in a photodetector containing the p -type ferroelectric semiconductor SbSI [28]. Unfortunately, in these experiments on the PGE, the electrodes and semiconductors are nonmagnetic, and the photocurrent is not spin polarized. Therefore, there currently lacks experimental study regarding the impact of magnetic electrodes on tuning the spin-polarized transport properties of the PGE photocurrent, which severely hinders the application of the PGE in spintronics, and, hence, theoretical investigations and simulations are rather desirable.

In a previous paper [15], we investigated the spin-polarized transport properties of the PGE in a 2D $\text{VSi}_2\text{N}_4/\text{WSi}_2\text{N}_4/\text{VSi}_2\text{N}_4$ (V-W-V) photodetector by using the method [29,30] based on the nonequilibrium Green's function formalism combined with density functional theory (NEGF-DFT) [31]. A 100% spin polarization can be obtained with the magnetic VSi_2N_4 electrodes. However, the mechanism for the perfect spin polarization is not discussed, and the influence of electrode-semiconductor interfaces on the spin-dependent transport properties of the photocurrent cannot be fully explored since only one kind of electrode (i.e., VSi_2N_4) was considered.

In this paper, we study the PGE in the 2D photodetectors composed of the $\text{VSi}_2\text{N}_4/\text{MoSi}_2\text{N}_4/\text{VSi}_2\text{N}_4$ (V-Mo-V) and $\text{NbSi}_2\text{N}_4/\text{MoSi}_2\text{N}_4/\text{NbSi}_2\text{N}_4$ (Nb-Mo-Nb) lateral heterojunctions, respectively, and reveal the role of electrode-semiconductor interfaces in determining the spin-dependent

*Contact author: yqxie@shnu.edu.cn

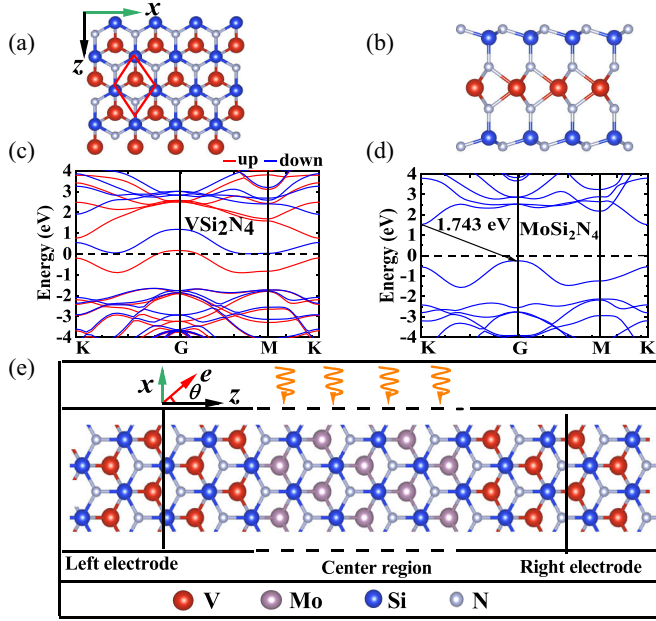


FIG. 1. (a) Top and (b) side views of the VSi_2N_4 monolayer, where the red parallelogram in panel (a) indicates the primitive cell. (c), (d) The electronic band structures of the VSi_2N_4 and MoSi_2N_4 monolayers, respectively. (e) Top view of the $\text{VSi}_2\text{N}_4/\text{MoSi}_2\text{N}_4/\text{VSi}_2\text{N}_4$ photodetector. The wavy curves indicate linearly polarized light that shines on MoSi_2N_4 in the center region, and vector \mathbf{e} is the polarization vector, which forms an angle θ with respect to the z direction.

transport properties of the PGE photocurrent. In the photodetectors, a MoSi_2N_4 monolayer is sandwiched between the two half-metallic electrodes composed of 2D VSi_2N_4 (NbSi_2N_4). The MoSi_2N_4 monolayer has a high electron and hole mobility [32], as well as large visible light absorption [33]. The VSi_2N_4 and NbSi_2N_4 electrodes have the different work function, which leads to an opposite band bending of the conduction bands in MoSi_2N_4 . This severely influences the magnitude, spin-injection efficiency (SIE) and magnetoresistance ratio of the PGE photocurrent in the two photodetectors, demonstrating the significance of magnetic electrodes in tuning the PGE.

II. MODEL AND METHODS

The VSi_2N_4 , NbSi_2N_4 , and MoSi_2N_4 monolayers have D_{3h} symmetry with similar lattice constants of 2.883, 2.965, and 2.909 Å, respectively. Figures 1(a) and 1(b) show top and side views of the VSi_2N_4 monolayer, where the primitive unit cell is indicated by a red parallelogram. Figure 1(c) shows the electronic band structures of VSi_2N_4 . It can be seen that the spin-up bands have metallic properties, as the Fermi energy level crosses the spin-up valence band (red solid lines) at G point in the Brillouin zone, while the spin-down bands (the blue-solid lines) show semiconductivity with a band gap of 1.643 eV. This indicates that the VSi_2N_4 monolayer is a half metal. The NbSi_2N_4 monolayer also shows a half-metallic behavior [34]. Figure 1(d) gives the electronic band structures of the MoSi_2N_4 monolayer, which is a nonmagnetic

semiconductor with a band gap of 1.743 eV. These results are in good agreement with our previous study [15].

The electronic band structures of VSi_2N_4 , MoSi_2N_4 , and NbSi_2N_4 are calculated with the DS-PAW package [35,36]. The exchange-correlation potentials are approximated using the generalized-gradient-approximation functional as parametrized by the Perdew, Burke, and Ernzerhof (PBE) functional [37]. Brillouin-zone integration is performed with a $21 \times 21 \times 1$ mesh of Monkhorst-Pack k points for geometry optimization and self-consistent electronic structure calculations. The kinetic-energy cutoff for the plane-wave basis is 600 eV. All the atoms in the unit cell are fully relaxed until the force on each atom is less than 10^{-4} eV/Å, and the convergence criterion for energy in the self-consistent field cycle is 10^{-5} eV.

Figure 1(e) shows the top view of the V-Mo-V photodetector, which is located in the x - z plane, and a 27 Å vacuum layer is added in the y direction to remove interactions between periodical image cells. The photodetector contains the left and right electrodes composed of the half-metallic VSi_2N_4 , and the center region formed by MoSi_2N_4 sandwiched between the half-metallic VSi_2N_4 . The two electrodes extend to $z = \pm\infty$, respectively, to mimic semi-infinite electrodes, while the whole device is periodical in the x direction. In the calculation of all electronic properties of the device, the VSi_2N_4 electrodes are treated as 2D monolayers. The MoSi_2N_4 monolayer in the center region is irradiated by linearly polarized light, as indicated by the wavy arrows in Fig. 1(e). The magnetic moments of VSi_2N_4 electrodes can be in a parallel configuration (PC) and antiparallel configuration (APC). The photocurrent flows along the z (armchair) direction from the left electrode through the center region to the right electrode. Using this device model, we can calculate the photocurrent generated in the PGE under the illumination of linearly polarized light.

Based on linear-response theory [38,39], we developed a method to calculate the PGE photocurrent in a device using the NEFG-DFT [31]. Specifically, for linearly polarized light, the photocurrent injecting into the left electrode can be written as [15,29]

$$J_L^{(\text{ph})} = \frac{ie}{h} \int \left\{ \cos^2 \theta \text{Tr} \left\{ \Gamma_L \left[G_1^{<(\text{ph})} + f_L (G_1^{>(\text{ph})} - G_1^{<(\text{ph})}) \right] \right\} \right. \\ \left. + \sin^2 \theta \text{Tr} \left\{ \Gamma_L \left[G_2^{<(\text{ph})} + f_L (G_2^{>(\text{ph})} - G_2^{<(\text{ph})}) \right] \right\} \right. \\ \left. + 2 \sin(2\theta) \text{Tr} \left\{ \Gamma_L \left[G_3^{<(\text{ph})} + f_L (G_3^{>(\text{ph})} - G_3^{<(\text{ph})}) \right] \right\} \right\} dE, \quad (1)$$

where $G_1^{>(\text{ph})}$, $G_2^{>(\text{ph})}$, $G_3^{>(\text{ph})}$ ($G_1^{<(\text{ph})}$, $G_2^{<(\text{ph})}$, $G_3^{<(\text{ph})}$) denote the greater (lesser) Green's functions including electron-photon interactions, which is determined by photon frequency, polarization vector \mathbf{e} and symmetry. Moreover, $\mathbf{e} = \cos \theta \mathbf{e}_1 + \sin \theta \mathbf{e}_2$ is the polarization vector of linearly polarized light, where θ is the angle formed by the polarization direction with respect to the vector \mathbf{e}_1 . The incidence direction of the light is determined by the vector product $\mathbf{e}_1 \times \mathbf{e}_2$. For normal incidence, polarized light shines vertically on the monolayer MoSi_2N_4 in the center region along the y axis and the polarization plane is in the x - z plane. In this case, the polarization vector \mathbf{e} forms a polarization angle θ with respect to the z direction, as indicated in Fig. 1(e). Consequently, we can

rewrite Eq. (1) as

$$J_L^{(\text{ph})} = \frac{ie}{\hbar} \int \text{Tr}\{\Gamma_L[G_4^{<(\text{ph})} + f_L(G_4^{>(\text{ph})} - G_4^{<(\text{ph})})]\}dE, \quad (2)$$

where

$$\begin{aligned} G_4^{>/<(\text{ph})} = & C_0 \cos^2 \alpha \sin^2 \theta (G_0^r p_x^\dagger G_0^{>/<} p_x G_0^a) \\ & + C_0 \sin^2 \alpha \sin^2 \theta (G_0^r p_y^\dagger G_0^{>/<} p_y G_0^a) \\ & + \frac{C_0}{2} \cos \alpha \sin(2\theta) (G_0^r p_z^\dagger G_0^{>/<} p_x G_0^a \\ & + G_0^r p_x^\dagger G_0^{>/<} p_z G_0^a) \\ & + \frac{C_0}{2} \sin \alpha \sin(2\theta) (G_0^r p_z^\dagger G_0^{>/<} p_y G_0^a \\ & + G_0^r p_y^\dagger G_0^{>/<} p_z G_0^a) \\ & + C_0 \sin(2\alpha) \cos^2 \theta (G_0^r p_y^\dagger G_0^{>/<} p_x G_0^a \\ & + G_0^r p_x^\dagger G_0^{>/<} p_y G_0^a) \\ & + C_0 \sin^2 \theta (G_0^r p_z^\dagger G_0^{>/<} p_z G_0^a). \end{aligned} \quad (3)$$

Equation (3) describes the dependence of the PGE photocurrent on both the incidence angle α and the polarization angle θ , which is determined by material symmetry. Here,

$$C_0 = (e/m_0)^2 \frac{\hbar \sqrt{u_r \varepsilon_r}}{2\omega \varepsilon c} I_\omega,$$

where e and m_0 are the electronic charge and bare electron mass, respectively; I_ω is the photon flux, which is defined as the number of photons per unit time per unit area, ω and c are the frequency and speed of light, respectively. μ_r is the relative magnetic susceptibility, ε_r is the relative dielectric constant. And ε is the dielectric constant. N is the number of photons. In the above expressions, $G_0^{r(a)}$ are the retarded or advanced Green's functions without photons, $G_0^{>/<}$ are the greater or lesser Green's functions without photons. The photocurrent can be normalized as $I = J_L^{(\text{ph})}/eI_\omega$ which still has dimensions of area, i.e., a_0^2/photon , where a_0 is the Bohr radius.

The above method to calculate the PGE photocurrent is implemented in the quantum transport package NanoDCAL, and in the following all the calculations are performed using NanoDCAL [31,38,39]. In the electronic self-consistent calculations for the electrodes and the center region, the Brillouin zone is sampled using $10 \times 1 \times 100$ and $10 \times 1 \times 1$ grids of k points, respectively. In the photocurrent transport calculation, $20 \times 1 \times 1$ k points are used. The double-zeta-polarized atomic-orbital basis is used to expand all the physical quantities, the exchange and correlation are treated at the level of the generalized-gradient-approximation functional as parametrized by the PBE, and the atomic cores are defined by the standard norm-conserving nonlocal pseudopotentials.

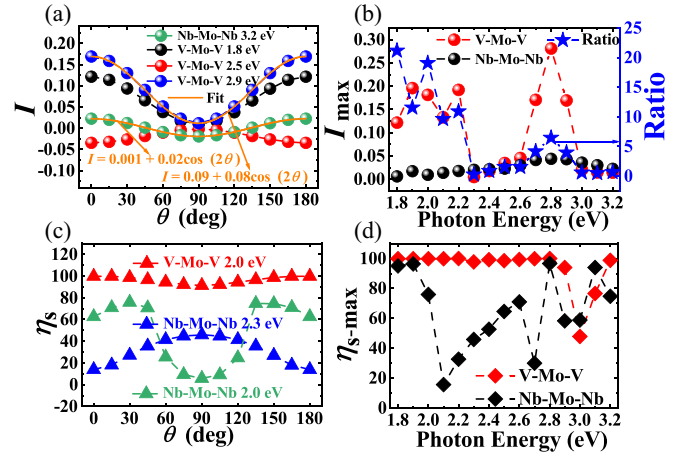


FIG. 2. (a) The variation of the photocurrent with the polarization angle θ at different photon energies for the V-Mo-V and Nb-Mo-Nb photodetectors, respectively. (b) The maximum photocurrent (I_{\max}) and the ratio of I_{\max} (blue stars) between the two photodetectors. (c) The variation of the SIE with θ at different photon energies and (d) the maximum SIE varying with photon energies for the two photodetectors.

III. RESULTS AND DISCUSSION

A. Photogalvanic effect in the V-Mo-V and Nb-Mo-Nb photodetectors

The PGE is generated when the central region is illuminated by linearly polarized light due to C_{2v} symmetry of the two devices. We consider the photon energies from 1.8 to 3.2 eV, and then calculate the photocurrent at intervals of 0.1 eV for normal incidence. To discuss the spin-dependent transport properties of the photocurrent, we define the SIE as

$$\eta_s = \frac{||I_\uparrow| - |I_\downarrow||}{|I_\uparrow| + |I_\downarrow|} \times 100\%, \quad (4)$$

where I_\uparrow and I_\downarrow denote the spin-polarized photocurrent contributed by spin-up and spin-down channels, respectively. η_s measures the degree of spin polarization in the photodetector. Once I_\uparrow or I_\downarrow disappears, $\eta_s = 100\%$, resulting in a fully-spin-polarized photocurrent, which means a perfect spin-filtering effect.

We first study the variation of the photocurrent with the polarization angle θ for different photon energies when the magnetic moments of the two electrodes are in the PC. We find that, for both the V-Mo-V and Nb-Mo-Nb photodetectors, the photocurrent shows a cosine dependence on θ , with a form $I = I_0 + A \cos(2\theta)$. Figure 2(a) gives the photocurrent as a function of θ for photon energies of 1.8, 2.5, and 2.9 eV for the V-Mo-V and of 3.2 eV for the Nb-Mo-Nb, respectively. It also shows that the photocurrents of 2.9 eV (blue spheres) and 3.2 eV (green spheres) can be fitted very well with functions $I = 0.09 + 0.08 \cos(2\theta)$ and $I = 0.001 + 0.02 \cos(2\theta)$ (see the orange lines), respectively. We then obtain a maximum photocurrent I_{\max} for each photon energy at either $\theta = 0^\circ$ or 90° , and compare I_{\max} between the two devices, as shown in Fig. 2(b). It can be seen that I_{\max} of the V-Mo-V photodetector (the red spheres) is overall larger than that of the Nb-Mo-Nb (the black spheres), e.g., in the photon-energy range from 1.8

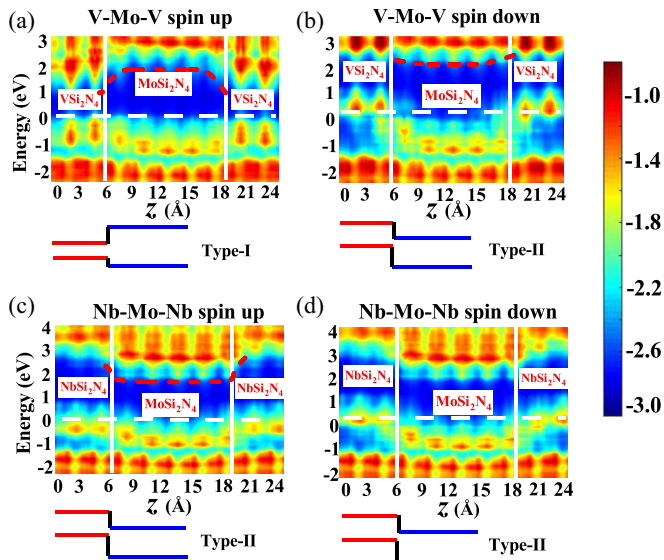


FIG. 3. (a), (b) The logarithmic LDOS of spin-up and spin-down electrons in the center region of the V-Mo-V photodetector, respectively. (c), (d) Spin-up and spin-down LDOS of the Nb-Mo-Nb photodetector, respectively. The white solid lines indicate the V(Nb)Si₂N₄/MoSi₂N₄ interface. The Fermi level is set at 0 eV, indicated by the white dashed line. Red dashed lines indicate the band bending of the conduction bands of the MoSi₂N₄ monolayer. The solid red and blue lines depict the band alignments.

to 2.2 eV. The maximum ratio (the blue stars) between I_{\max} of the two devices is 21 at 1.8 eV.

Next, we study the variation of the SIE (η_s) with the polarization angle θ for the PC. We find that, for the V-Mo-V photodetector, η_s varies slightly with θ and maintains a high value up to 100% for most of the photon energies. As an example, Fig. 2(c) shows η_s as a function of θ at photon energy of 2.0 eV for the V-Mo-V (the red triangles). In contrast, for the Nb-Mo-Nb, η_s varies severely with θ , and is significantly smaller than that of the V-Mo-V for most of the photon energies, as shown in Fig. 2(c). We then compare the maximum η_s at each photon energies for the two devices, as shown in Fig. 2(d). It shows that for most of the photon energies $\eta_{s-\max}$ of the V-Mo-V device (almost) reaches 100% (e.g., from 1.8 to 2.8 eV) and is evidently larger than that of the Nb-Mo-Nb. This means that the fully-spin-polarized photocurrent can be produced in the V-Mo-V photodetector within a broad photon energy range. We now obtain that the V-Mo-V photodetector can produce a larger photocurrent with a higher SIE than the Nb-Mo-Nb photodetector in a broad photon energy range.

To understand these results, we discuss the band alignments and charge transfer between the half-metallic V(Nb)Si₂N₄ electrodes and the semiconducting MoSi₂N₄ for the two devices. Figure 3(a) gives the local density of states (LDOS) of the spin-up electrons in the center region of the V-Mo-V photodetector along the transport (z) direction. The VSi₂N₄/MoSi₂N₄ interface is indicated by the white solid lines, and the Fermi energy level is set at 0 eV, indicated by a white dashed line. It can be seen that the Fermi level is very close to the top valence band of MoSi₂N₄, indicating a p -type

doping. Notably, the LDOS shows that the conduction bands of MoSi₂N₄ have an evident downward band bending at the VSi₂N₄/MoSi₂N₄ interface, as indicated by the red dashed line. This is a typical band bending at the metal/ p -type-semiconductor interface, as the work function of the metallic VSi₂N₄ (5.43 eV) is lower than that of the semiconducting MoSi₂N₄ (5.49 eV), according to our calculations. It means that the photoexcited spin-up electrons encounter no potential barrier when transferring from MoSi₂N₄ to the VSi₂N₄ electrodes, which generates a larger spin-up photocurrent. However, the spin-down LDOS of MoSi₂N₄ in the V-Mo-V photodetector has a slight upward band bending, as indicated by the red dashed line in Fig. 3(b). This means that the photoexcited spin-down electrons in MoSi₂N₄ have to tunnel through a barrier into the electrodes, and therefore leads to a smaller spin-down photocurrent. Consequently, the spin-up photocurrent is much larger than the spin-down photocurrent, leading to a high SIE with η_s up to 100% for most of the photon energies. For the Nb-Mo-Nb photodetector, the spin-up LDOS demonstrates an evident upward band bending, as indicated by the red dashed line in Fig. 3(c), since the work function of the NbSi₂N₄ electrodes (5.76 eV) is greater than that of MoSi₂N₄. In addition, the spin-down LDOS also shows an upward band bending [Fig. 3(d)]. Therefore, for the Nb-Mo-Nb photodetector, both spin-up and spin-down electrons have to tunnel through a large barrier into the electrodes, which leads to a reduced photocurrent with a lower η_s , as compared with the V-Mo-V photodetector.

The band bending corresponds to the different band alignments of the two interfaces. For the VSi₂N₄/MoSi₂N₄ interface, the spin-up band alignment has the type-I shape [Fig. 3(a)], while the spin-down band alignment is of the type-II shape [Fig. 3(b)]. In contrast, for the NbSi₂N₄/MoSi₂N₄ interface, both the spin-up and spin-down alignments are of the type-II shape [Figs. 3(c) and 3(d)]. Such band alignments agree with those obtained by comparing the individual band structures of the 2D VSi₂N₄, NbSi₂N₄, and MoSi₂N₄ monolayers, as shown in Figs. S2 and S3 (See Supplemental Material [40]). It is thus conclude that a type-I band alignment tends to lead to a larger photocurrent due to the zero-tunneling barrier for the photoexcited electrons, while a type-II band alignment causes a small photocurrent due to the finite barrier height. It is the different band alignment for the spin-up (type-I) and spin-down (type-II) electrons that eventually leads to a larger photocurrent with a high SIE (up to 100%) for the V-Mo-V photodetector.

The band-bending of the conduction bands of MoSi₂N₄ originates from the charge redistribution when the MoSi₂N₄ monolayer forms an interface with the V(Nb)Si₂N₄ electrodes. Figure 4 shows the contour plot of the charge-density in the x - z plane for the V-Mo-V photodetector. We find that the V₁ atom in the VSi₂N₄ electrode has a larger charge density ($6.620e/a_0^3$) than the V₂ atom ($6.460e/a_0^3$) in the VSi₂N₄/MoSi₂N₄ interface, and the Mo₁ atom close to the interface has a larger charge density ($4.173e/a_0^3$) than the Mo₂ atom ($4.158e/a_0^3$) in the center region [Fig. 4(b)]. This suggests that electrons transfer from the metallic VSi₂N₄ to the p -type semiconductor MoSi₂N₄, which lifts the potential energy of MoSi₂N₄ at the interface, leading to the downward band bending of the conduction bands of MoSi₂N₄ [see

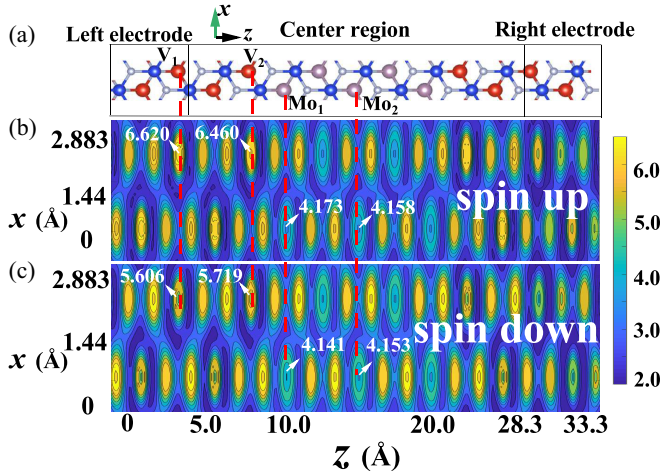


FIG. 4. (a) Device model of the V-Mo-V photodetector, and the contour plot in the x - z plane for the (b) spin-up and (c) spin-down charge-densities of the V-Mo-V photodetector, respectively. The red dashed lines indicate the locations of different atoms in the photodetector.

Fig. 3(a)]. In contrast, for the spin-down charge density, we find that the V_1 atom has a smaller charge density ($5.606 e/a_0^3$) than the V_2 atom ($5.719 e/a_0^3$), while the Mo_1 atom has a smaller charge density than the Mo_2 atom [Fig. 4(c)]. It means that the spin-down electrons transfer from $MoSi_2N_4$ to VSi_2N_4 in the interface, which lowers the potential energy of the $MoSi_2N_4$ and leads to the upward band bending of the conduction bands [see Fig. 3(b)].

The band bending of the Nb-Mo-Nb photodetector can also be understood from the charge distribution. Figure 5 shows the contour plot of the charge density in the x - z plane for the Nb-Mo-Nb photodetector. We find that, for the spin-up electrons [Fig. 5(b)], the Nb_1 atom has a smaller charge density ($3.538 e/a_0^3$) than the Nb_2 atom ($3.565 e/a_0^3$) in the $NbSi_2N_4/MoSi_2N_4$ interface, and the Mo_1 atom also has

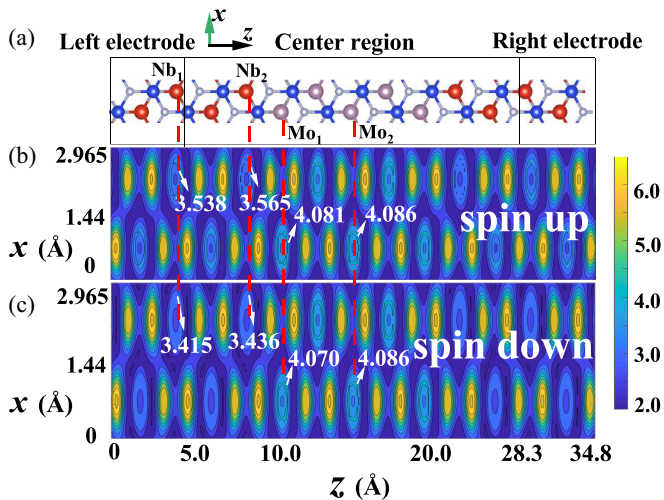


FIG. 5. (a) Device model of the Nb-Mo-Nb photodetector, and the contour plot in the x - z plane for the (b) spin-up and (c) spin-down charge-densities of the Nb-Mo-Nb photodetector, respectively. The red dashed lines indicate the different atoms in the photodetector.

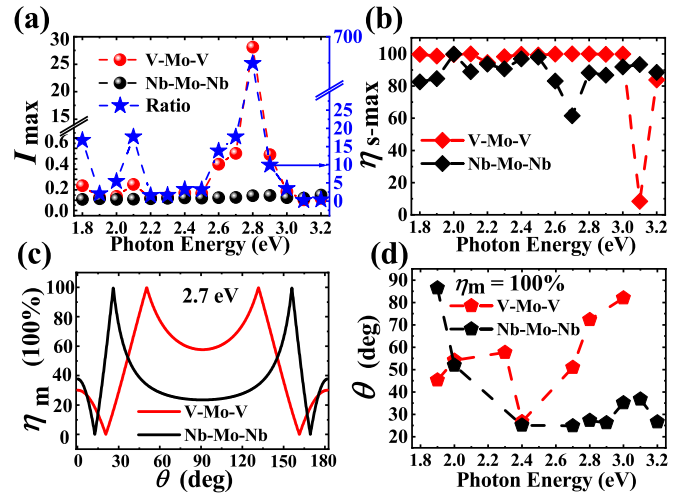


FIG. 6. (a) The maximum photocurrent (I_{max}) for the V-Mo-V and Nb-Mo-Nb photodetectors in the APC, and the ratio of I_{max} (blue stars) between the two photodetectors. (b) The maximum SIE (η_{s-max}) varying with photon energies for the two photodetectors. (c) The magnetoresistance ratio (η_m) as a function of θ . (d) The photon energy and θ , at which $\eta_m = 100\%$, for the two photodetectors, respectively.

a smaller charge density ($4.081 e/a_0^3$) than the Mo_2 atom ($4.086 e/a_0^3$) in the center region [see Fig. 5(b)]. The same is true for the spin-down electrons, as shown in Fig. 5(c). This means that both the spin-up and spin-down electrons transfer from $MoSi_2N_4$ to $NbSi_2N_4$ at the interface, which lowers the potential energy of the $MoSi_2N_4$ and leads to the upward band-bending of the conduction bands, as shown in Figs. 3(c) and 3(d).

Finally, we investigate the photocurrent when the magnetic moments of the two electrodes are in the APC. Figures 6(a) and 6(b) show that I_{max} and η_{s-max} of the V-Mo-V photodetector are larger than those of the Nb-Mo-Nb photodetector for most of the photon energies, similarly to the case of the PC [see Figs. 2(b) and 2(d)]. Moreover, we calculate the magnetoresistance ratio of the photocurrent, which is defined as

$$\eta_m = \frac{||I_{PC} - I_{APC}||}{|I_{PC} + I_{APC}|} \times 100\%, \quad (5)$$

where I_{PC} and I_{APC} are the photocurrents in the PC and APC, respectively. Then a maximum η_m (100%) is achieved when either I_{PC} or I_{APC} vanishes. We find that η_m varies with the polarization angle θ [Fig. 6(c)] and reaches 100% at a certain θ for a number of photon energies, as shown in Fig. 6(d), which means a perfect spin-valve effect is achieved.

B. Discussion

The dependence of the PGE photocurrent on θ is exclusively determined by material symmetry. According to phenomenological theory [16,41–43], the photocurrent can be written as [44,45]

$$J_\lambda = \Sigma_{\mu\nu} \chi_{\lambda\mu\nu} (E_\mu E_\nu^* + E_\nu E_\mu^*)/2, \quad (6)$$

where χ is the third-order tensors that are dependent on the photon energy and material symmetry, E_μ and E_ν denote the

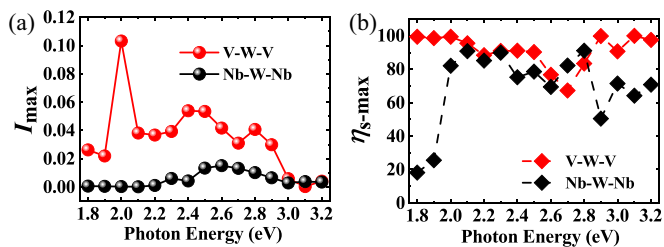


FIG. 7. Comparison of the (a) photocurrent and (b) SIE ($\eta_{s-\max}$) between the V-W-V and Nb-W-Nb photodetectors.

three components of the light electrical field. λ , μ , and ν represent the three components of the Cartesian coordinates. In our model, the photodetectors are located in the x - z plane, and the photocurrent I flows along the z axis (armchair direction). For a material with C_{2v} symmetry, the tensor χ has several components, i.e., χ_{xx} , χ_{yy} , χ_{zz} , χ_{xy} , χ_{yz} , χ_{zx} , χ_{zy} , χ_{zz} . However, only χ_{xx} , χ_{yy} , and χ_{zz} contribute to J_z . At normal incidence (parallel to the y axis), $E_x = E_0 \sin \theta$, $E_z = E_0 \cos \theta$, $E_y = 0$. We obtain the photocurrent along the z axis:

$$\begin{aligned} J_z &= \sum_{\mu\nu} \chi_{\lambda\mu\nu} (E_\mu E_\nu^* + E_\nu E_\mu^*)/2 \\ &= \chi_{xxx} (E_x E_x^* + E_x E_x^*)/2 \\ &\quad + \chi_{zzz} (E_z E_z^* + E_z E_z^*)/2 \\ &= \chi_{xxx} E_0^2 \sin^2 \theta + \chi_{zzz} E_0^2 \cos^2 \theta. \end{aligned} \quad (7)$$

Equation (7) shows that the photocurrent J_z has a $\cos(2\theta)$ dependence on the polarization angle θ at normal incidence, which is in good agreement with our calculations, as shown in Fig. 2(a).

In previous papers, we studied the PGE in the V-W-V [15] and NbSi₂N₄-WSi₂N₄-NbSi₂N₄ (Nb-W-Nb) photodetectors [46]. According to our calculations, the work function of WSi₂N₄ (5.50 eV) is larger than that of VSi₂N₄ (5.43 eV), while is lower than that of NbSi₂N₄ (5.76 eV). This indicates

that the V-W-V photodetector should have a larger photocurrent with a higher SIE as compared with Nb-W-Nb. We then compare the magnitude of the photocurrent and the SIE between the two photodetectors, as shown in Fig. 7. It can be seen that, for most of the photon energies, both the magnitude and SIE of the photocurrent of the V-W-V photodetector are indeed larger than those of the Nb-W-Nb photodetector. These findings provide a further evidence that the band alignment of the electrode-semiconductor interface plays a critical role in determining the magnitude and spin-transport properties of the photocurrent in the PGE. Figure S4 of the Supplemental Material [40] gives the band alignments of the V(Nb)Si₂N₄/WSi₂N₄ interface, which are similar to those of V(Nb)Si₂N₄/MoSi₂N₄ interface.

IV. CONCLUSIONS

In summary, we study the PGE in the V-Mo-V and Nb-Mo-Nb photodetectors under illumination of linear polarized light by using quantum transport simulations. In a broad visible range, both the magnitude and SIE of the V-Mo-V photodetector are much larger than those of the Nb-Mo-Nb photodetector, while both the photodetectors can possess a high magnetoresistance ratio. Our results reveal that band alignment at the electrode-semiconductor interface can significantly influence not only the magnitude but also the spin-polarization of the photocurrent in the PGE. Therefore, by using electrodes with an appropriate work function, both the magnitude and SIE of the PGE photocurrent can be largely enhanced, and a perfect spin-valve effect can be achieved, showing the potential of the PGE for spintronic devices.

ACKNOWLEDGMENTS

This work is supported by the National Natural Science Foundation of China under Grant No. 51871156. We gratefully acknowledge HZWTECH for providing computation facilities.

- [1] L. Li, P. Yuan, T. Liu, Z. Ma, C. Xia, and X. Li, Self-powered broadband photodetector based on a monolayer InSe p - i - n homojunction, *Phys. Rev. Appl.* **19**, 014039 (2023).
- [2] N. Sun, H. Ye, W. Zhou, R. Yang, R. Quhe, Y. Liu, and Z. Chen, Enhanced photogalvanic effect in MoSSe monolayer with grain boundaries, *Appl. Phys. Lett.* **123**, 211107 (2023).
- [3] C. Niu, S. Y. Huang, N. Ghosh, P. K. Tan, M. Y. Wang, W. Z. Wu, X. F. Xu, and P. D. Ye, Tunable circular photogalvanic and photovoltaic effect in 2D tellurium with different chirality, *Nano Lett.* **23**, 8 (2023).
- [4] W. Y. Wu, J. L. Yu, Y. Y. Jiang, X. L. Zeng, Y. H. Chen, Y. Liu, C. M. Yin, S. Y. Cheng, Y. F. Lai, K. He, and Q. K. Xue, Tuning of circular photogalvanic effect of surface states in the topological insulator Sb₂Te₃ via structural deformation, *Appl. Phys. Lett.* **120**, 062407 (2022).
- [5] B. Kim, N. Park, and J. Kim, Giant bulk photovoltaic effect driven by the wall-to-wall charge shift in WS₂ nanotubes, *Nat. Commun.* **13**, 3237 (2022).
- [6] X. Jiang, L. Kang, J. F. Wang, and B. Huang, Giant bulk electrophotovoltaic effect in heteronodal-line systems, *Phys. Rev. Lett.* **130**, 256902 (2023).
- [7] Z. B. Dai and A. M. Rappe, Magnetic bulk photovoltaic effect: Strong and weak field, *Phys. Rev. B* **107**, L201201 (2023).
- [8] A. Ebrahimian, M. Dadsetani, and R. Asgari, Shift current in molecular crystals possessing charge-transfer characteristics, *Phys. Rev. Appl.* **19**, 044006 (2023).
- [9] A. Abdelsamie, L. You, L. Wang, S. Li, M. Gu, and J. Wang, Crossover between bulk and interface photovoltaic mechanisms in a ferroelectric vertical heterostructure, *Phys. Rev. Appl.* **17**, 024047 (2022).
- [10] Y. R. Chang, R. Nanae, S. Kitamura, T. Nishimura, H. N. Wang, Y. B. Xiang, K. Shinokita, K. Matsuda, T. Taniguchi, K. Watanabe, and K. Nagashio, Shift-current photovoltaics based on a non-centrosymmetric phase in in-plane ferroelectric SnS, *Adv. Mater.* **35**, 2301172 (2023).
- [11] S. H. Wang, H. Zhang, J. Zhang, S. Q. Li, D. B. Luo, J. Y. Wang, K. X. Jin, and J. R. Sun, Circular photogalvanic effect in oxide two-dimensional electron gases, *Phys. Rev. Lett.* **128**, 187401 (2022).
- [12] H. Ishizuka and M. Sato, Large photogalvanic spin current by magnetic resonance in bilayer Cr trihalides, *Phys. Rev. Lett.* **129**, 107201 (2022).

- [13] R. Fei, W. Song, L. P. Nazzaro, and L. Yang, PT-symmetry-enabled spin circular photogalvanic effect in antiferromagnetic insulators, *Phys. Rev. Lett.* **127**, 207402 (2021).
- [14] Y. Z. Luo, Y. Q. Xie, J. Zhao, Y. B. Hu, X. Ye, and S. H. Ke, Perfect in-plane CrI₃ spin-valve driven by photogalvanic effect, *Phys. Rev. Mater.* **5**, 054004 (2021).
- [15] L. Shu, L. Y. Qian, X. Ye, and Y. Q. Xie, Multifunctional two-dimensional VSi₂N₄/WSi₂N₄/VSi₂N₄ photodetector driven by the photogalvanic effect, *Phys. Rev. Appl.* **17**, 054010 (2022).
- [16] J. Wang, Y. Y. Huang, Z. Lei, Y. Y. Xi, W. Y. Du, X. Q. Cao, Y. Q. Ge, L. P. Zhu, Y. X. Zhou, and X. L. Xu, Tunable polarized terahertz wave generation induced by spontaneous polarization-dependent ultrafast shift current from vertically grown ferroelectric SnS, *Phys. Rev. B* **106**, 235308 (2022).
- [17] S. M. Young and A. M. Rappe, First principles calculation of the shift current photovoltaic effect in ferroelectrics, *Phys. Rev. Lett.* **109**, 116601 (2012).
- [18] L. Z. Tan and A. M. Rappe, Upper limit on shift current generation in extended systems, *Phys. Rev. B* **100**, 085102 (2019).
- [19] S. M. Young, F. Zheng, and A. M. Rappe, First-principles calculation of the bulk photovoltaic effect in bismuth ferrite, *Phys. Rev. Lett.* **109**, 236601 (2012).
- [20] P. Pieri and G. C. Strinati, Strong-coupling limit in the evolution from BCS superconductivity to Bose-Einstein condensation, *Phys. Rev. B* **61**, 15370 (2000).
- [21] C. M. Zhang, P. Guo, and J. Zhou, Tailoring bulk photovoltaic effects in magnetic sliding ferroelectric materials, *Nano Lett.* **22**, 9297 (2022).
- [22] Z. Qian, J. Zhou, H. Wang, and S. Liu, Shift current response in elemental two-dimensional ferroelectrics, *npj Comput. Mater.* **9**, 67 (2023).
- [23] F. Xu, H. Su, Z. Gong, Y. Wei, H. Jin, and H. Guo, Controllable ferroelectricity and bulk photovoltaic effect in elemental group-V monolayers through strain engineering, *Phys. Rev. B* **106**, 195418 (2022).
- [24] S. Shen, H. Ai, Y. Ma, H. Bai, X. Du, F. Li, and H. Pan, In-plane ferroelectric monolayer TiNbX₄O and its application in bulk photovoltaic effect, *Appl. Phys. Lett.* **123**, 052901 (2023).
- [25] S. Dhara, E. J. Mele, and R. Agarwal, Voltage-tunable circular photogalvanic effect in silicon nanowires, *Science* **349**, 726 (2015).
- [26] Y. J. Zhang, T. Ideue, M. Onga, F. Qin, R. Suzuki, A. Zak, R. Tenne, J. H. Smet, and Y. Iwasa, Enhanced intrinsic photovoltaic effect in tungsten disulfide nanotubes, *Nature (London)* **570**, 349 (2019).
- [27] J. Quereda, J. Hidding, T. S. Ghiasi, B. J. van Wees, C. H. van der Wal, and M. H. D. Guimarães, The role of device asymmetries and Schottky barriers on the helicity-dependent photoresponse of 2D phototransistors, *npj 2D Mater. Appl.* **5**, 13 (2021).
- [28] M. Nakamura, H. Hatada, Y. Kaneko, N. Ogawa, Y. Tokura, and M. Kawasaki, Impact of electrodes on the extraction of shift current from a ferroelectric semiconductor SbSI, *Appl. Phys. Lett.* **113**, 232901 (2018).
- [29] Y. Q. Xie, L. Zhang, Y. Zhu, L. Liu, and H. Guo, Photogalvanic effect in monolayer black phosphorus, *Nanotechnol.* **26**, 455202 (2015).
- [30] G. L. Lin, Y. Q. Xie, L. Shu, and X. Ye, Large switchable circular photogalvanic effect in the narrow-band-gap InSe/In₂Se₃ ferroelectric heterojunction, *Phys. Rev. Appl.* **20**, 034035 (2023).
- [31] J. Taylor, H. Guo, and J. Wang, *Ab initio* modeling of quantum transport properties of molecular electronic devices, *Phys. Rev. B* **63**, 245407 (2001).
- [32] Y. L. Hong, Z. B. Liu, L. Wang, T. Y. Zhou, W. Ma, C. Xu, S. Feng, L. Chen, M. L. Chen, D. M. Sun, X. Q. Chen, H. M. Cheng, and W. C. Ren, Chemical vapor deposition of layered two-dimensional MoSi₂N₄ materials, *Science* **369**, 670 (2020).
- [33] B. Mortazavi, B. Javvaji, F. Shojaei, T. Rabczuk, A. V. Shapeev, and X. Y. Zhuang, Exceptional piezoelectricity, high thermal conductivity and stiffness and promising photocatalysis in two-dimensional MoSi₂N₄ family confirmed by first-principles, *Nano Energy* **82**, 105716 (2021).
- [34] A. Yadav, J. Kangsabanik, N. Singh, and A. Alam, Novel two-dimensional MA₂N₄ materials for photovoltaic and spintronic applications, *J. Phys. Chem. Lett.* **12**, 10120 (2021).
- [35] P. E. Blöchl, Projector augmented-wave methods, *Phys. Rev. B* **50**, 17953 (1994).
- [36] For details of the DS-PAW first-principles plane-wave package, see <http://iresearch.net.cn/web/product-service?id=10>.
- [37] J. P. Perdew, K. Burke, and M. Ernzerhof, Generalized gradient approximation made simple, *Phys. Rev. Lett.* **78**, 1396 (1997).
- [38] L. E. Henrickson, Nonequilibrium photocurrent modeling in resonant tunneling photodetectors, *J. Appl. Phys.* **91**, 6273 (2002).
- [39] L. Zhang, K. Gong, J. Z. Chen, L. Liu, Y. Zhu, D. Xiao, and H. Guo, Generation and transport of valley-polarized current in transition-metal dichalcogenides, *Phys. Rev. B* **90**, 195428 (2014).
- [40] See Supplemental Material at <http://link.aps.org/supplemental/10.1103/PhysRevMaterials.8.074002> for calculation details, energy band structures, band alignments and photocurrent of the enlarged devices.
- [41] T. Rangel, B. M. Fregoso, B. S. Mendoza, T. Morimoto, J. E. Moore, and J. B. Neaton, Large bulk photovoltaic effect and spontaneous polarization of single-layer monochalcogenides, *Phys. Rev. Lett.* **119**, 067402 (2017).
- [42] W. Weber, L. E. Golub, S. N. Danilov, J. Karch, C. Reitmaier, B. Wittmann, V. V. Belkov, E. L. Ivchenko, Z. D. Kvon, N. Q. Vinh, A. F. G. van der Meer, B. Murdin, and S. D. Ganichev, Quantum ratchet effects induced by terahertz radiation in GaN-based two-dimensional structures, *Phys. Rev. B* **77**, 245304 (2008).
- [43] M. M. Glazov, S. D. Ganichev, High frequency electric field induced nonlinear effects in graphene, *Phys. Rep.* **535**, 101 (2014).
- [44] J. E. Sipe and A. J. Shkrebtii, Second-order optical response in semiconductors, *Phys. Rev. B* **61**, 5337 (2000).
- [45] J. L. Yu, Y. H. Chen, S. Y. Cheng, and Y. F. Lai, Spectra of circular and linear photogalvanic effect at inter-band excitation in In_{0.15}Ga_{0.85}As/Al_{0.3}Ga_{0.7}As multiple quantum wells, *Physica E (Amsterdam, Neth.)* **49**, 92 (2013).
- [46] L. Shu, Y. M. Wang, and Y. Q. Xie, Photogalvanic effect of the two-dimensional magnetic NbSi₂N₄/WSi₂N₄/NbSi₂N₄ heterojunction, *J. Shanghai Normal Univ. (Nat. Sci.)* **52**, 688 (2023).